Article

Low-Thrust Nonlinear Orbit Control for Very Low Lunar Orbits

Edoardo Maria Leonardi [1,*], Mauro Pontani [1], Stefano Carletta [2] and Paolo Teofilatto [2]

1   Department of Astronautical, Electrical, and Energy Engineering, Sapienza University of Rome, via Salaria 851, 00138 Rome, Italy; mauro.pontani@uniroma1.it
2   School of Aerospace Engineering, Sapienza University of Rome, via Salaria 851, 00138 Rome, Italy; stefano.carletta@uniroma1.it (S.C.); paolo.teofilatto@uniroma1.it (P.T.)
*   Correspondence: edoardomaria.leonardi@uniroma1.it

Abstract: In the next decades, both space agencies and private competitors are targeting the lunar environment as a scientific and technological resource for future space missions. In particular, the confirmed existence of water-ice deposits in the vicinity of the poles (predominantly the south pole) makes polar or near-polar low lunar orbits attractive for the purpose of designing space missions that could search for suitable Lunar base sites. However, traveling very-low-altitude orbits is very challenging, as they are strongly perturbed by the Moon's gravity field as well as third- and fourth-body effects due to the Earth and the Sun. Several studies demonstrate that these orbits are expected to impact the lunar surface in a few months. Therefore, the definition and implementation of an effective station-keeping strategy represents a crucial issue in order to extend satellites' lifetime. In this paper, a feedback nonlinear control law is employed in order to perform corrective maneuvers aimed at keeping the state of the satellite within acceptable margins. The satellite is assumed to be equipped with a steerable and throttleable low-thrust propulsion system. The control law is based on the Lyapunov stability theory and does not require any reference path to track, with a considerable decrease in the computational cost. The proposed real-time control law includes control saturation, related to the maximum available thrust magnitude, and is developed employing modified equinoctial elements, in order to avoid singularities and extend its range of application. Finally, the strategy at hand is tested in the presence of all the relevant perturbations (i.e., harmonics of the selenopotential, third- and fourth-body effects) in order to show its effectiveness and efficiency.

Keywords: low lunar orbits; low-thrust propulsion; real-time guidance; feedback control; Lyapunov theory

1. Introduction

In recent years, space mission analysis and design in cislunar space has attracted an increasing interest among space agencies and private actors in the space economy. In particular, the ARTEMIS program led by NASA, in collaboration with the European Space Agency and other international partners, is foreseeing the construction of an orbital outpost along a Near-Rectilinear-Halo-Orbit (NRHO) to conduct scientific research in deep space and in a following phase to support the human exploration of the Moon [1].

Lunar satellite constellations are being proposed for a variety of purposes, including telecommunications, navigation, and remote sensing. However, lunar orbits are greatly perturbed by the gravitational harmonics of the selenopotential. To mitigate this issue, former research suggested the use of a variety of frozen orbits [2,3]. However, if the spacecraft travels very-low-altitude orbits, then sectoral and tesseral harmonics play a significant role, and lead to differential perturbing actions on each satellite, depending on its longitude (and, ultimately, on its initial right ascension of the ascending node [4]). For these reasons, maintenance along very low lunar orbits is an open problem of practical interest. Station-keeping maneuvers along quasi-frozen, near-polar, and extremely low-altitude lunar orbits were investigated by Singh et al. through impulsive maneuvers,

though the authors suggested investigating the use of continuous low-thrust for correction station-keeping maneuvers [5]. A low-thrust propulsion system is instead employed by Liu et al. to achieve lifetime extension of ultra low-altitude lunar spacecraft [6]. However, they identified the formulation of a complete mission scenario, including orbit transfers in cislunar space, as the next step in the research.

From a technological point of view, the greater complexity of lunar missions and space vehicles will require the ability of the different subsystems to autonomously handle a larger amount of operations, especially for guidance, navigation, and control (GNC) tasks [7]. For example, the exploration vehicle Orion is equipped with a far larger autonomy and automation with respect to the Space Shuttle or the International Space Station, as it is required to autonomously perform rendezvous and docking operations or the deorbit burn [8]. Therefore, the design of future space vehicles must guarantee the autonomous execution of all GNC functions [9]. This involves the necessity to address two compelling requirements: first, develop a guidance algorithm able to manage a complex dynamical environment, which is nonlinear and highly perturbed, resulting in the inadequacy of Keplerian-based algorithms [7]; second, determine suitable techniques that can be implemented on an onboard software with limited computational resources.

The present research focuses on nonlinear orbit control for orbit acquisition and maintenance by employing low thrust. Low-thrust orbit transfer can be achieved through optimal control, via either direct or indirect methods, which constitutes the bulk of most of previous research on this topic. With this regard, Conway summarized several methods suitable for trajectory optimization problems [10]. However, optimal control is a time-demanding task that is usually accomplished offline, and thus, it cannot fulfill the necessity of a real-time low-thrust orbit maneuvering algorithm. Instead, feedback methods provide closed-loop control laws that can be employed for autonomous guidance, navigation, and control schemes [11]. For example, Kluever proposed a simple guidance scheme based on optimal control laws that maximize the time rate of the orbital elements according to the variational equations, suitable for an onboard implementation [12]. Gurfil investigated the problem of orbital transfer under continuous low thrust and obtained a nonlinear feedback controller by showing the accessibility of Gauss variational Equations [13]. Chang et al. employed Lyapunov stability theory in order to derive a feedback controller [14], while Leeghim et al. revisited the latter work to avoid crashing the planet surface during large-angle maneuvers and including the shadow effect [15]. However, these previous works take into consideration Keplerian trajectories and do not address the influence of perturbations.

Recently, machine learning has been proposed as an effective strategy to develop lightweight and computationally efficient guidance algorithms, suitable for onboard software. In this context, neural networks have been applied to autonomous spacecraft guidance problems for proximity operations and low-thrust orbit transfers [16–18]. Although the use of neural networks enhances real-time guidance capabilities, there are still some issues. First of all, this technology relies on an extensive training, which is computationally expensive and can be only achieved through ground-based resources. This may limit the autonomy when a spacecraft must face new challenging scenarios, especially for missions that require limited ground support. On the other hand, nonlinear control provides a feedback law with guaranteed analytic stability within its convergence domain. Therefore, it is capable of providing online feasible trajectories without any reference path nor offline information except for gains, which is often more important than optimality [9]. Furthermore, the appropriate tuning of the parameters allows obtaining solutions that are very close to those found with optimization techniques [19,20].

The aim of this study is to employ a saturated feedback control law to acquire a spacecraft in a very-low-altitude lunar orbit and to drive it toward a desired operational orbit, not necessarily designed as a frozen path. Similar very-low-altitude lunar orbits may represent interesting options for the deployment of constellations, provided that coordinated control of the orbit elements is feasible. In this study, orbital motion is described

in terms of modified equinoctial elements, which are nonsingular in most operational scenarios [21]. All relevant perturbations are included in the dynamical model, i.e., several harmonics of the selenopotential and third body gravitational attraction due to the Sun and the Earth, whose orbital motion is described in an ephemeris model. The spacecraft is assumed to be equipped with a low-thrust engine, which allows considerable propellant saving, with respect to a high-thrust propulsion system, at the price of a longer maneuver time. In particular, two different target operational orbits are considered: (i) a circular orbit with assigned radius; (ii) an elliptic orbit with specified minimum radius at periselenium and maximum radius at aposelenium. A similar feedback control law is employed also in previous works [22–24], and is here extended to focus on the following aspects:

- The boundary conditions are being formulated in terms of modified equinoctial elements, with several positive analytical consequences;
- The stability analysis is being extended to target orbits with time-varying orbit elements.

In the end, this research has the ultimate intent of extending the range of applicability of nonlinear orbit control, thus paving the way for its use in challenging, highly perturbed mission scenarios, such as low-thrust correction maneuvers in very low lunar orbits.

2. Orbit Dynamics

An accurate description of the orbital dynamics requires a proper definition of an inertial frame. As a preliminary step, the Moon Centered Inertial frame (MCI) is introduced, with unit vectors $(\hat{c}_1^M, \hat{c}_2^M, \hat{c}_3^M)$ defined as follows: (i) $\hat{c}_1^M$ lies in the Moon equatorial plane and is coplanar with the line that connects the Earth and the Moon at a reference time t_{ref}, directed toward the far side of the Moon; (ii) $\hat{c}_3^M$ is aligned with the Moon rotation axis at t_{ref}; (iii) $\hat{c}_2^M$ completes the right-handed set. The Local Vertical Local Horizontal (LVLH) frame is instead aligned with unit vectors $(\hat{r}, \hat{\theta}, \hat{h})$: (i) $\hat{r}$ is directed from the Moon center to the instantaneous position of the vehicle; (ii) $\hat{h}$ is aligned with the spacecraft angular momentum; (iii) $\hat{\theta}$ completes the right-handed set. If $\mathbf{R}_i(\alpha)$ denotes an elementary rotation matrix by angle α about axis i, then the two reference frames can be linked through three successive rotations,

$$\begin{bmatrix} \hat{r} \\ \hat{\theta} \\ \hat{h} \end{bmatrix} = \mathbf{R}_3(\omega + \theta)\mathbf{R}_1(i)\mathbf{R}_3(\Omega) \begin{bmatrix} \hat{c}_1^M \\ \hat{c}_2^M \\ \hat{c}_3^M \end{bmatrix}, \tag{1}$$

where Ω is the Right Ascension of the Ascending Node (RAAN), i the inclination of the orbital plane, ω the argument of periselenium, and θ the true anomaly. Furthermore, we introduce the Local Horizontal (LH) frame, associated with unit vectors $(\hat{r}, \hat{E}, \hat{N})$, where $\hat{E}$ and $\hat{N}$ are aligned with the local (lunar) East and North directions, respectively. If ζ is the heading angle, then the following relation holds,

$$\begin{bmatrix} \hat{r} \\ \hat{\theta} \\ \hat{h} \end{bmatrix} = \mathbf{R}_1(\zeta) \begin{bmatrix} \hat{r} \\ \hat{E} \\ \hat{N} \end{bmatrix}. \tag{2}$$

Figure 1 shows the reference frames and related angles. The spacecraft is modeled as a point mass and its motion is mainly affected by the Moon gravitational field. The presence of perturbing effects is also addressed: (i) the gravitational pull of Earth and Sun; (ii) the relevant harmonics of the selenopotential (down to two orders of magnitude less than the largest harmonic term J_2), that is, those associated with coefficients $|J_{lm}| > 10^{-6}$. Appendix A collects all planetary data employed in this research. The gravitational influ-

ence of the Earth and Sun can be modeled as third body perturbations following Battin–Giorgi approach ([25,26]):

$$\vec{a}_{3i} = -\frac{\mu_i}{\|\vec{r}_i\|^3 (q_i+1)^{3/2}} \left(\vec{r} + \vec{r}_i q_i \frac{q_i^2 + 3q_i + 3}{(q_i+1)^{3/2}+1}\right), \quad q_i := \frac{\vec{r}\cdot\vec{r} - 2\vec{r}\cdot\vec{r}_i}{\vec{r}_i\cdot\vec{r}_i}, \quad (3)$$

where $\vec{r}_i$ denotes the vector position of the i-body with respect to the Moon and $\vec{r}$ the instantaneous position vector of the spacecraft with respect to the central body.
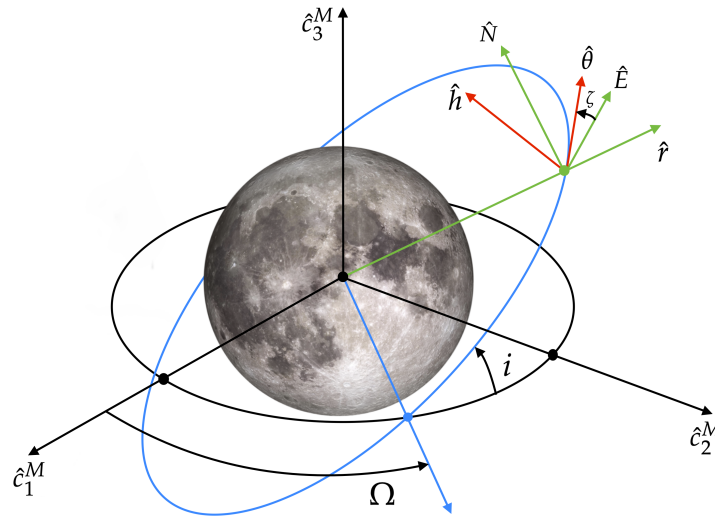

Figure 1. MCI and LVLH frames.

Instead, the selenopotential U can be expanded in terms of Legendre polynomials $P_{l,m}$,

$$U = \frac{\mu_m}{r} - \frac{\mu_m}{r}\sum_{l=2}^{\infty}\left(\frac{R_m}{l}\right)^l J_l P_{l0}(sin\phi) + \frac{\mu_m}{r}\sum_{l=2}^{\infty}\sum_{m=1}^{l}\left(\frac{R_m}{r}\right)^l J_{l,m} P_{l,m}(\sin\phi)\cos\left[m(\lambda_g - \lambda_{l,m})\right], \quad (4)$$

where R_m is the lunar equatorial radius, ϕ the geographical latitude and λ_g the geographical longitude, and the coefficients (J_{lm} and λ_{lm}) of zonal, tesseral, and sectoral harmonics are provided by the Lunar Prospector LP100K model for the Moon gravitational field [27]. Then, the gravitational acceleration can be computed in the LH-frame,

$$\vec{g} = \nabla U, \quad \text{where } \nabla = \hat{r}\frac{\partial}{\partial r} + \frac{\hat{E}}{r\cos\phi}\frac{\partial}{\partial\lambda_g} + \frac{\hat{N}}{r}\frac{\partial}{\partial\phi}. \quad (5)$$

Finally, by means of Equation (2), it is straightforward to obtain the components of the perturbing acceleration in the LVLH-frame. The strongest gravitational perturbation is associated with the coefficient J_2. It is useful to express the perturbing acceleration due to the zonal harmonic J_2 in the LVLH-frame,

$$\vec{a}_{J_2} = \frac{3\mu_m}{r^4}R_m^2 J_2 \begin{bmatrix} \dfrac{3\sin^2(\omega+\theta)\sin^2 i - 1}{2} \\ -\sin^2 i \sin(\omega+\theta)\cos(\omega+\theta) \\ -\sin i \cos i \sin(\omega+\theta) \end{bmatrix}^T \begin{bmatrix} \hat{r} \\ \hat{\theta} \\ \hat{h} \end{bmatrix} = \begin{bmatrix} a_r^{J_2} & a_\theta^{J_2} & a_h^{J_2} \end{bmatrix}\begin{bmatrix} \hat{r} \\ \hat{\theta} \\ \hat{h} \end{bmatrix}, \quad (6)$$

where μ_m is the Moon gravitational parameter. The J_2 harmonic is responsible for the time variation of the orbital elements, as predicted by the well-known Gauss equations [28],

$$\dot{p} = 2\sqrt{\frac{p}{\mu_m}} r a_\theta^{J_2}, \tag{7}$$

$$\dot{e} = \sqrt{\frac{p}{\mu_m}} a_r^{J_2} \sin\theta + \sqrt{\frac{p}{\mu_m}} a_\theta^{J_2} \frac{e + e\cos^2\theta + 2\cos\theta}{1 + e\cos\theta}, \tag{8}$$

$$\dot{i} = r a_\theta^{J_2} \frac{\cos(\omega + \theta)}{h}, \tag{9}$$

$$\dot{\Omega} = r a_h^{J_2} \frac{\sin(\omega + \theta)}{h\sin i}, \tag{10}$$

$$\dot{\omega} = -r a_h^{J_2} \frac{\sin(\omega + \theta)\cos i}{h\sin i} - \frac{a_r^{J_2}}{e}\cos\theta\sqrt{\frac{p}{\mu_m}} + a_\theta^{J_2}\sqrt{\frac{p}{\mu_m}}\sin\theta\frac{e\cos\theta + 2}{e(1 + e\cos\theta)}, \tag{11}$$

$$\dot{\theta} = \sqrt{\frac{\mu_m}{p^3}}(1 + e\cos\theta)^2 + \frac{a_r^{J_2}}{e}\cos\theta\sqrt{\frac{p}{\mu_m}} - a_\theta^{J_2}\sqrt{\frac{p}{\mu_m}}\sin\theta\frac{e\cos\theta + 2}{e(1 + e\cos\theta)}, \tag{12}$$

where p is the semilatus rectum and e the eccentricity. However, it is possible to apply averaging techniques in order to filter short period oscillations. This procedure yields the average time derivatives of the orbital elements, which equal zero for the semimajor axis, the eccentricy, and the inclination. Instead, the RAAN, the argument of pericenter and the true anomaly exhibit a secular variation. Therefore, the proposed strategy is to employ the control effort to maintain a constant semimajor axis, eccentricity and inclination, while complying with the variation of the RAAN, argument of pericenter and true anomaly, in order to achieve propellant saving.

The orbit dynamics can be described by means of modified equinoctial elements x_i, $i = 1, \ldots, 6$,

$$x_1 = a(1 - e^2), \tag{13}$$

$$x_2 = e\cos(\Omega + \omega), \tag{14}$$

$$x_3 = e\sin(\Omega + \omega), \tag{15}$$

$$x_4 = \tan\frac{i}{2}\cos\Omega, \tag{16}$$

$$x_5 = \tan\frac{i}{2}\sin\Omega, \tag{17}$$

$$x_6 = \Omega + \omega + \theta, \tag{18}$$

where a is the semi-major axis. This set of elements is well-suited for numerical integration, as it does not exhibit singularities for every keplerian trajectories, with the exception of equatorial retrograde orbits. Given the vector of non Keplerian accelerations $\boldsymbol{a} = \begin{bmatrix} a_r & a_\theta & a_h \end{bmatrix}^T$ expressed in the LVLH frame and $\boldsymbol{x} := \begin{bmatrix} x_1 & x_2 & x_3 & x_4 & x_5 \end{bmatrix}^T$, the dynamical equations can be written as

$$\dot{\boldsymbol{x}} = \mathbf{G}(\boldsymbol{x}, x_6)\boldsymbol{a}, \tag{19}$$

where $\eta = 1 + x_2 \cos x_6 + x_3 \sin x_6$ and

$$\mathbf{G} = \sqrt{\frac{x_1}{\mu_m}} \begin{bmatrix} 0 & \dfrac{2x_1}{\eta} & 0 \\[2mm] \sin x_6 & \dfrac{(1+\eta)\cos x_6 + x_2}{\eta} & -\dfrac{x_4 \sin x_6 - x_5 \cos x_6}{\eta}x_3 \\[2mm] -\cos x_6 & \dfrac{(1+\eta)\sin x_6 + x_3}{\eta} & \dfrac{x_4 \sin x_6 - x_5 \cos x_6}{\eta}x_2 \\[2mm] 0 & 0 & \dfrac{1 + x_4^2 + x_5^2}{2\eta}\cos x_6 \\[2mm] 0 & 0 & \dfrac{1 + x_4^2 + x_5^2}{2\eta}\sin x_6 \end{bmatrix}. \tag{20}$$

The dynamical equation for the orbital element x_6 is instead given by

$$\dot{x}_6 = \sqrt{\frac{\mu_m}{x_1^3}}\eta^2 + \sqrt{\frac{x_1}{\mu_m}}\frac{x_4 \sin x_6 - x_5 \cos x_6}{\eta}a_h. \tag{21}$$

Finally, if T denotes the instantaneous thrust magnitude and m_0 the initial mass, the dynamical equation for the mass ratio x_7 can be obtained,

$$\dot{x}_7 = -\frac{u_T}{c}, \quad \text{with} \quad u_T = \frac{T}{m_0}, \tag{22}$$

where c is the effective exhaust velocity of the propulsion system. The thrust can be modulated up to its maximum value T_{max}, and thus $0 \le u_T \le u_{Tmax} = T_{max}/m_0$.

3. Nonlinear Orbit Control

The aim of this section is to introduce a nonlinear feedback control law able to perform an initial orbit acquisition and keep the spacecraft along the desired orbit.

3.1. Formulation of the Problem

Nonlinear orbit control is proposed as an effective strategy to drive a spacecraft toward a specified orbit (with subsequent maintenance), starting from a different initial orbit. As described in Section 2, the main effect the J_2 harmonic is to yield a secular variation in the orbital elements (Ω, ω, θ). Therefore, the state is integrated numerically by assigning the time variation of the desired orbital elements $(a_d, e_d, i_d, \Omega_d(t), \omega_d(t), \theta_d(t))$,

$$\dot{a}_d = \dot{e}_d = \dot{i}_d = 0, \tag{23}$$

while $\dot{\Omega}_d$, $\dot{\omega}_d$, and $\dot{\theta}_d$ are given according to Equations (10)–(12). Then, through analytical differentiation, it is straightforward to convert the time variation of the classical orbital elements into equinoctial elements,

$$\dot{x}_{1d} = \dot{a}_d(1 - e_d^2) - 2e_d\dot{e}_d a_d = 0, \tag{24}$$

$$\dot{x}_{2d} = \dot{e}_d \cos(\Omega_d + \omega_d) - (\dot{\Omega}_d + \dot{\omega}_d)e_d \sin(\Omega_d + \omega_d) = 0, \tag{25}$$

$$\dot{x}_{3d} = \dot{e}_d \sin(\Omega_d + \omega_d) + (\dot{\Omega}_d + \dot{\omega}_d)e_d \cos(\Omega_d + \omega_d) = 0, \tag{26}$$

$$\dot{x}_{4d} = -\tan\left(\frac{i_d}{2}\right)\dot{\Omega}_d \sin\Omega_d + \frac{1}{2\cos^2 i_d}\dot{i}_d \cos\Omega_d, \tag{27}$$

$$\dot{x}_{5d} = \tan\left(\frac{i_d}{2}\right)\dot{\Omega}_d \cos\Omega_d + \frac{1}{2\cos^2 i_d}\dot{i}_d \sin\Omega_d, \tag{28}$$

$$\dot{x}_{6d} = \dot{\Omega}_d + \dot{\omega}_d + \dot{\theta}_d, \tag{29}$$

where subscript d refers to the desired value of the equinoctial element. Equations (24) through (29) can be integrated to yield the time history of the desired orbit.

3.2. Feedback Control Law

The operational orbit conditions can be enforced as a nonlinear constraint,

$$\boldsymbol{\Psi}(x, t) = \begin{bmatrix} \Psi_1 \\ \Psi_2 \\ \Psi_3 \end{bmatrix} = \mathbf{0}. \tag{30}$$

Specifically, the components of the constraint can be expressed as

$$\Psi_1 = (x_1 - x_{1d})^2 = 0, \tag{31}$$

$$\Psi_2 = (x_2 - x_{2d})^2 + (x_3 - x_{3d})^2 = 0, \tag{32}$$

$$\Psi_3 = (x_4 - x_{4d})^2 + (x_5 - x_{5d})^2 = 0. \tag{33}$$

The first component Ψ_1 corresponds to a constraint on the semilatus rectum,

$$\Psi_1 = (p - p_d)^2. \tag{34}$$

Instead, the second component Ψ_2 pursues the desired eccentricity of the orbit,

$$(x_2 - x_{2d})^2 + (x_3 - x_{3d})^2 =$$
$$[e \cos(\Omega + \omega) - e_d \cos(\Omega_d + \omega_d)]^2 + [e \sin(\Omega + \omega) - e_d \sin(\Omega_d + \omega_d)]^2 =$$
$$= e^2 + e_d^2 - 2 e e_d \cos(\Omega - \Omega_d + \omega - \omega_d). \tag{35}$$

Finally, we can prove that component Ψ_3 fixes the orientation of the orbital plane. Indeed, let us denote with $\vec{h}$ and $\vec{h}_d$ the actual and desired angular momentum unit vectors as expressed in the MCI-frame,

$$\vec{h} = \begin{bmatrix} \sin\Omega \sin i \\ \cos\Omega \sin i \\ \cos i \end{bmatrix}^T \begin{bmatrix} \hat{c}_1^M \\ \hat{c}_2^M \\ \hat{c}_3^M \end{bmatrix} = \begin{bmatrix} \dfrac{2x_5}{1 + x_4^2 + x_5^2} \\ \dfrac{2x_4}{1 + x_4^2 + x_5^2} \\ \dfrac{1 - x_4^2 - x_5^2}{1 + x_4^2 + x_5^2} \end{bmatrix}^T \begin{bmatrix} \hat{c}_1^M \\ \hat{c}_2^M \\ \hat{c}_3^M \end{bmatrix}, \tag{36}$$

$$\vec{h}_d = \begin{bmatrix} \sin\Omega_d \sin i_d \\ \cos\Omega_d \sin i_d \\ \cos i_d \end{bmatrix}^T \begin{bmatrix} \hat{c}_1^M \\ \hat{c}_2^M \\ \hat{c}_3^M \end{bmatrix} = \begin{bmatrix} \dfrac{2x_{5d}}{1 + x_{4d}^2 + x_{5d}^2} \\ \dfrac{2x_{4d}}{1 + x_{4d}^2 + x_{5d}^2} \\ \dfrac{1 - x_{4d}^2 - x_{5d}^2}{1 + x_{4d}^2 + x_{5d}^2} \end{bmatrix}^T \begin{bmatrix} \hat{c}_1^M \\ \hat{c}_2^M \\ \hat{c}_3^M \end{bmatrix}. \tag{37}$$

Then, the alignment condition between the actual and the desired orbital plane can be expressed as a scalar product,

$$\vec{h} \cdot \vec{h}_d = 1. \tag{38}$$

By expanding the scalar product, we obtain

$$2x_4 x_{4d} + 2x_5 x_{5d} + (1 - x_4^2 - x_5^2)(1 - x_{4d}^2 - x_{5d}^2) = (1 + x_4^2 + x_5^2)(1 + x_{4d}^2 + x_{5d}^2). \tag{39}$$

Equation (39) can be easily simplified into

$$-2x_4x_{4d} - 2x_5x_{5d} + x_4^2 + x_5^2 + x_{4d}^2 + x_{5d}^2 = (x_4 - x_{4d})^2 + (x_5 - x_{5d})^2 = 0. \tag{40}$$

Equations (31)–(33) define the target set. In order to achieve the desired final conditions, a nonlinear control law is identified through the definition of a meaningful Lyapunov function,

$$V = \frac{1}{2}\mathbf{\Psi}^T\mathbf{K}\mathbf{\Psi}, \tag{41}$$

where $\mathbf{K}$ is a symmetric and positive definite matrix. It is straightforward to recognize that $V > 0$ unless $\mathbf{\Psi} = \mathbf{0}$. Let us introduce the auxiliary vectors

$$\boldsymbol{b} = \mathbf{G}^T\left(\frac{\partial\mathbf{\Psi}}{\partial x}\right)^T\mathbf{K}\mathbf{\Psi}, \tag{42}$$

$$\boldsymbol{d} = \boldsymbol{a}_P + \left(\frac{\partial\mathbf{\Psi}}{\partial x}\mathbf{G}\right)^{-1}\frac{\partial\mathbf{\Psi}}{\partial t}, \tag{43}$$

where $\boldsymbol{a}_P$ denotes the total perturbing acceleration. Then, as already proven in reference [23], the following nonlinear control law leads the dynamical system to converge to the target state, provided that $\mathbf{\Psi}$ and $\frac{\partial\mathbf{\Psi}}{\partial x}$ are continuous, $\left[(\partial\mathbf{\Psi}/\partial x\,\mathbf{G})\right]^{-1}(\partial\mathbf{\Psi}/\partial t)$ is finite, $|\boldsymbol{b}| > 0$ unless $\mathbf{\Psi} = \mathbf{0}$, and $u_{Tmax} > x_7|\boldsymbol{d}|$:

$$\boldsymbol{u}_T = -u_T\frac{\boldsymbol{b}+\boldsymbol{d}}{|\boldsymbol{b}+\boldsymbol{d}|}, \quad \text{with} \tag{44}$$

$$u_T = \begin{cases} x_7|\boldsymbol{b}+\boldsymbol{d}|, & \text{if } x_7|\boldsymbol{b}+\boldsymbol{d}| \leq u_{Tmax} \\ 0, & \text{if } x_7|\boldsymbol{b}+\boldsymbol{d}| > u_{Tmax} \text{ and } \boldsymbol{b}^T\boldsymbol{b} + \boldsymbol{b}^T\mathbf{d} < 0 \\ u_{Tmax}, & \text{if } x_7|\boldsymbol{b}+\boldsymbol{d}| > u_{Tmax} \text{ and } \boldsymbol{b}^T\boldsymbol{b} + \boldsymbol{b}^T\mathbf{d} \geq 0. \end{cases} \tag{45}$$

The attracting set contains all the dynamical states that fulfill $\dot{V} = 0$, that is, if all the components of $\boldsymbol{b}$ are zero regardless of any choice of the gain coefficients (k_1, k_2, k_3). Thus, the attracting set must be investigated in order to guarantee asymptotic stability via the Lyapunov theorem. Equations (46)–(3.2) show the analytical expression of the components of vector $\boldsymbol{b}$, denoted with (b_1, b_2, b_3),

$$b_1 = -2k_2\Psi_2\sqrt{\frac{x_1}{\mu_m}}\Big[(x_3 - x_{3d})\cos x_6 - (x_2 - x_{2d})\sin x_6\Big], \tag{46}$$

$$b_2 = 4k_1\Psi_1\frac{x_1 - x_{1d}}{\eta}\sqrt{\frac{x_1^3}{\mu_m}} +$$

$$2k_2\sqrt{\frac{x_1}{\mu_m}}\frac{\Psi_2}{\eta}\Big\{(x_2 - x_{2d})[x_2 + (1+\eta)\cos x_6] + (x_3 - x_{3d})[x_3 + (1+\eta)\sin x_6]\Big\}, \tag{47}$$

$$b_3 = 2k_2\sqrt{\frac{x_1}{\mu_m}}\frac{\Psi_2}{\eta}(x_5\cos x_6 - x_4\sin x_6)\Big[(x_2 - x_{2d})x_3 - (x_3 - x_{3d})x_2\Big]$$

$$+k_3\Psi_3\sqrt{\frac{x_1}{\mu_m}}\frac{1 + x_4^2 + x_5^2}{\eta}\Big[(x_4 - x_{4d})\cos x_6 + (x_5 - x_{5d})\sin x_6\Big]. \tag{48}$$

First of all, it is straightforward to recognize that if $x_1 = 0$ (rectilinear trajectories), $b_1 = b_2 = b_3 = 0$. If $x_1 \neq 0$, then $b_1 = 0$ if either $\Psi_2 = 0$ or

$$(x_3 - x_{3d})\cos x_6 - (x_2 - x_{2d})\sin x_6 = 0. \tag{49}$$

The latter relation is satisfied regardless of x_6 (which is time-varying also along the desired orbit) only if $x_2 = x_{2d}$ and $x_3 = x_{3d}$, which is equivalent to $\Psi_2 = 0$. This implies that also $b_2 = 0$ if and only if $\Psi_1 = 0$. Finally, $b_3 = 0$ regardless of x_6 if either $\Psi_3 = 0$ or $x_4 = x_{4d}$ and

$x_5 = x_{5d}$, which is, however, equivalent to $\Psi_3 = 0$. To sum up, the attracting set includes the following subsets:

- $x_1 = 0$;
- $\Psi_1 = \Psi_2 = \Psi_3 = 0$ (target set).

However, as the condition $\boldsymbol{b} = 0$ implies $\dot{\boldsymbol{b}} = 0$, it is possible to rule out subset 1. Indeed, we have

$$\dot{b}_i = \frac{\partial b_i}{\partial \boldsymbol{x}}\dot{\boldsymbol{x}} + \frac{\partial b_i}{\partial x_6}\dot{x}_6 + \sum_{j=1}^{5}\frac{\partial b_i}{\partial x_{jd}}\dot{x}_{jd} = \frac{\partial b_i}{\partial \boldsymbol{x}}\boldsymbol{G}\boldsymbol{a} + \frac{\partial b_i}{\partial x_6}\dot{x}_6 + \sum_{j=1}^{5}\frac{\partial b_i}{\partial x_{jd}}\dot{x}_{jd}, \tag{50}$$

for $i = 1, 2, 3$. If we evaluate this expression when $\boldsymbol{a} = \boldsymbol{0}$, we obtain

$$\dot{b}_i = \frac{\partial b_i}{\partial x_6}\sqrt{\frac{\mu_m}{x_1^3}}\eta^2 + \sum_{j=1}^{5}\frac{\partial b_i}{\partial x_{jd}}\dot{x}_{jd}. \tag{51}$$

For simplicity, let us rename

$$b_1 = \Psi_2(x_2, x_{2d}, x_3, x_{3d})\sqrt{\frac{x_1}{\mu_m}}f_1(x_2, x_{2d}, x_3, x_{3d}, x_6), \tag{52}$$

$$b_2 = \Psi_1(x_1, x_{1d})\sqrt{\frac{x_1^3}{\mu_m}}f_2(x_1, x_{1d}, x_2, x_3, x_6)$$

$$+\Psi_2(x_2, x_{2d}, x_3, x_{3d})\sqrt{\frac{x_1}{\mu_m}}f_3(x_2, x_{2d}, x_3, x_{3d}, x_6), \tag{53}$$

$$b_3 = \Psi_2(x_2, x_{2d}, x_3, x_{3d})\sqrt{\frac{x_1}{\mu_m}}f_4(x_2, x_{2d}, x_3, x_{3d}, x_4, x_5, x_6)$$

$$+\Psi_3(x_4, x_{4d}, x_5, x_{5d})\sqrt{\frac{x_1}{\mu_m}}f_5(x_2, x_3, x_4, x_{4d}, x_5, x_{5d}, x_6), \tag{54}$$

where

$$f_1 = -2k_2\Big[(x_3 - x_{3d})\cos x_6 - (x_2 - x_{2d})\sin x_6\Big], \tag{55}$$

$$f_2 = 4k_1\frac{x_1 - x_{1d}}{\eta}, \tag{56}$$

$$f_3 = 2k_2\frac{(x_2 - x_{2d})\big[x_2 + (1 + \eta)\cos x_6\big] + (x_3 - x_{3d})\big[x_3 + (1 + \eta)\sin x_6\big]}{\eta}, \tag{57}$$

$$f_4 = 2k_2(x_5\cos x_6 - x_4\sin x_6)\Big[\frac{(x_2 - x_{2d})x_3 - (x_3 - x_{3d})x_2}{\eta}\Big], \tag{58}$$

$$f_5 = k_3\frac{1 + x_4^2 + x_5^2}{\eta}\Big[(x_4 - x_{4d})\cos x_6 + (x_5 - x_{5d})\sin x_6\Big]. \tag{59}$$

Therefore,

$$\dot{b}_1 = \Psi_2 \frac{\eta^2}{x_1} \frac{\partial f_1}{\partial x_6} + \sqrt{\frac{x_1}{\mu_m}} \left[\left(\frac{\partial \Psi_2}{\partial x_{2d}} f_1 + \Psi_2 \frac{\partial f_1}{\partial x_{2d}} \right) \dot{x}_{2d} + \left(\frac{\partial \Psi_2}{\partial x_{3d}} f_1 + \Psi_2 \frac{\partial f_1}{\partial x_{3d}} \right) \dot{x}_{3d} \right], \tag{60}$$

$$\dot{b}_2 = \Psi_1 \eta^2 \frac{\partial f_2}{\partial x_6} + \Psi_2 \frac{\eta^2}{x_1} \frac{\partial f_3}{\partial x_6} + \sqrt{\frac{x_1^3}{\mu_m}} \left(f_2 \frac{\partial \Psi_1}{\partial x_{1d}} + \Psi_1 \frac{\partial f_2}{\partial x_{1d}} \right) \dot{x}_{1d}$$
$$+ \sqrt{\frac{x_1}{\mu_m}} \left[\left(\frac{\partial \Psi_2}{\partial x_{2d}} f_3 + \Psi_2 \frac{\partial f_3}{\partial x_{2d}} \right) \dot{x}_{2d} + \left(\frac{\partial \Psi_2}{\partial x_{3d}} f_3 + \Psi_2 \frac{\partial f_3}{\partial x_{3d}} \right) \dot{x}_{3d} \right], \tag{61}$$

$$\dot{b}_3 = \left(\Psi_2 \frac{\partial f_4}{\partial x_6} + \Psi_3 \frac{\partial f_5}{\partial x_6} \right) \frac{\eta^2}{x_1}$$
$$+ \sqrt{\frac{x_1}{\mu_m}} \left[\left(\frac{\partial \Psi_2}{\partial x_{2d}} f_4 + \frac{\partial f_4}{\partial x_{2d}} \Psi_2 \right) \dot{x}_{2d} + \left(\frac{\partial \Psi_2}{\partial x_{3d}} f_4 + \frac{\partial f_4}{\partial x_{3d}} \Psi_2 \right) \dot{x}_{3d} \right]$$
$$+ \sqrt{\frac{x_1}{\mu_m}} \left[\left(\frac{\partial \Psi_3}{\partial x_{4d}} f_5 + \frac{\partial f_5}{\partial x_{4d}} \Psi_3 \right) \dot{x}_{4d} + \left(\frac{\partial \Psi_3}{\partial x_{5d}} f_5 + \frac{\partial f_5}{\partial x_{5d}} \Psi_3 \right) \dot{x}_{5d} \right]. \tag{62}$$

It is evident that, as investigated in [23], the subset associated with the rectilinear trajectories can be ruled out as the time derivative $\dot{b}$ diverges. Instead, it is straightforward to see that, when the target set is reached, the following relations hold:

$$f_1 = f_2 = f_3 = f_4 = f_5 = 0, \tag{63}$$

and therefore, $\dot{b} = \mathbf{0}$ as well. Since the invariant set does not contain other subsets than the target set, the asymptotic stability is quasi-global. Finally, the quantity $\left[(\partial \mathbf{\Psi}/\partial x) \, \mathbf{G} \right]^{-1} (\partial \mathbf{\Psi}/\partial t)$ must be investigated to check any singularity issue. Let us denote with $(\bar{d}_1, \bar{d}_2, \bar{d}_3)$ the components of vector $\mathbf{d} - \mathbf{a}_P$. First of all, component $\bar{d}_2$ is inspected. Using Mathematica [29], one can prove that

$$\lim_{\mathbf{x} \to \mathbf{x}_d} \bar{d}_2 = -\sqrt{\frac{\mu_m}{x_{1d}}} \dot{x}_{1d} \frac{(1 + x_{2d} \cos x_6 + x_{3d} \sin x_6)}{2 x_{1d}}, \tag{64}$$

which is finite if and only if $x_{1d} \neq 0$. Instead, the analytical expression for component $\bar{d}_1$ is

$$\bar{d}_1 = \sqrt{\frac{\mu_m}{x_1}} \frac{(x_2 - x_{2d}) \dot{x}_{2d} + (x_3 - x_{3d}) \dot{x}_{3d}}{(x_3 - x_{3d}) \cos x_6 - (x_2 - x_{2d}) \sin x_6}. \tag{65}$$

The relation for $\bar{d}_1$ can be written as

$$\bar{d}_1 = \sqrt{\frac{\mu_m}{x_1}} \left\{ \frac{\dot{x}_{2d}}{\frac{x_3 - x_{3d}}{x_2 - x_{2d}} \cos x_6 - \sin x_6} + \frac{\dot{x}_{3d}}{\cos x_6 - \frac{x_2 - x_{2d}}{x_3 - x_{3d}} \sin x_6} \right\}. \tag{66}$$

The following limits turn out to be indeterminate:

$$\lim_{x_2 \to x_{2d}, \; x_3 \to x_{3d}} \frac{x_2 - x_{2d}}{x_3 - x_{3d}}, \tag{67}$$

$$\lim_{x_2 \to x_{2d}, \; x_3 \to x_{3d}} \frac{x_3 - x_{3d}}{x_2 - x_{2d}}, \tag{68}$$

However, the following parameterization can be used as $x_2 \to x_{2d}$ and $x_3 \to x_{3d}$:

$$x_2 = x_{2d} + z_1 \tau, \tag{69}$$

$$x_3 = x_{3d} + z_2 \tau, \tag{70}$$

where τ is a parameter that tends to zero, whereas z_1 and z_2 are two constant values that identify the direction traveled as $x_2 \to x_{2d}$ and $x_3 \to x_{3d}$. This means that the following limits depend on the ratio z_1/z_2:

$$\lim_{x_2 \to x_{2d},\, x_3 \to x_{3d}} \frac{x_2 - x_{2d}}{x_3 - x_{3d}} = \frac{z_1}{z_2}, \tag{71}$$

$$\lim_{x_2 \to x_{2d},\, x_3 \to x_{3d}} \frac{x_3 - x_{3d}}{x_2 - x_{2d}} = \frac{z_2}{z_1}. \tag{72}$$

Therefore, the limit of Equation (66) as $x_2 \to x_{2d}$ and $x_3 \to x_{3d}$ depends on the direction (i.e., the ratio z_1/z_2) and is

$$\bar{d}_1 = \sqrt{\frac{\mu_m}{x_{1d}}} \left\{ \frac{\dot{x}_{2d}}{\dfrac{z_2}{z_1} \cos x_6 - \sin x_6} + \frac{\dot{x}_{3d}}{\cos x_6 - \dfrac{z_1}{z_2} \sin x_6} \right\}. \tag{73}$$

As x_6 is time varying, the component $\bar{d}_1$ still remains finite almost everywhere, provided $x_{1d} \neq 0$. Finally, component $\bar{d}_3$ is written as

$$\bar{d}_3 = -2\sqrt{\frac{\mu_m}{x_1}} \frac{\eta}{1 + x_4^2 + x_5^2} \left\{ \frac{(x_4 - x_{4d})\dot{x}_{4d} + (x_5 - x_{5d})\dot{x}_{5d}}{(x_4 - x_{4d})\cos x_6 + (x_5 - x_{5d})\sin x_6} \right\}. \tag{74}$$

The same considerations developed for Equation (66) still hold and ensure that the feedback law at hand is feasible.

4. Numerical Simulations

The spacecraft is assumed to be equipped with a low-thrust propulsion system, characterized by the effective exhaust velocity c and the maximum thrust acceleration u_{Tmax},

$$c = 30 \ \text{km/s}, \quad u_{Tmax} = 5 \cdot 10^{-5} g_0, \tag{75}$$

where $g_0 = 9.81 \ \text{m/s}^2$ is the gravity acceleration at sea level. Canonical units are employed for the numerical simulations; the distance unit (DU) is equal to the Moon radius, while the time unit (TU) is selected in order to obtain a unit gravitational parameter,

$$DU = 1738.1 \ \text{km}, \tag{76}$$

$$TU = \sqrt{\frac{1}{\mu_m} DU^3}. \tag{77}$$

The following weighting coefficients are employed:

$$k_1 = 10^5, \quad k_2 = 10^5, \quad k_3 = 10^7. \tag{78}$$

Two target orbits are selected, with a different inclination of the orbital plane. Table 1 collects the initial conditions for these two orbits. The initial argument of latitude is set to $10°$.

Table 1. Target orbits.

Orbital Element	i_d [deg]	$\Omega_{d,0}$ [deg]
Target orbit 1	60	300
Target orbit 2	90	300

Instead, the initial state of the spacecraft is specified by assigning a random value of the initial radii at periselenium (r_P^0) and aposelenium (r_A^0), selected using a stochastic uniform distribution over the following intervals:

$$r_P^0 \in [50, 100] \text{ km}, \tag{79}$$

$$r_A^0 \in [100, 500] \text{ km}. \tag{80}$$

Furthermore, the initial inclination and RAAN are chosen according to a normal distribution with mean value, respectively, i_d and Ω_d^0, and standard deviation is set to 5 deg.

For each target orbit, two different operational scenarios are analyzed: (i) final circular orbit at an altitude of 100 km; (ii) final elliptic orbit with assigned minimum periselenium radius ($r_{Pmin} = R_m + 50$ km) and maximum aposelenium radius ($r_{Amax} = R_m + 150$ km). The latter operational scenario can be specified through the following relations:

$$r_P = \frac{p}{1+e} \geq r_{Pmin} \rightarrow p \geq r_{Pmin}(1+e), \tag{81}$$

$$r_A = \frac{p}{1-e} \leq r_{Amax} \rightarrow p \leq r_{Amax}(1-e). \tag{82}$$

These two inequalities identify a triangular region in the (p, e) plane, where the motion of the spacecraft is constrained. In particular, after orbit injection, the propulsive effort is employed in order to release the vehicle inside this specific region and the thrust is turned off when the inequalities (81) and (82) are satisfied, together with

$$|\Psi_3| < 10^{-6}. \tag{83}$$

For each Monte Carlo campaign, 100 simulations are run. The initial reference epoch is set to 1 January 2025 and the total simulation time is about 1 year (370 days, 2 hours, 51 minutes). For each simulation, the mean values of the semimajor axis ($\bar{a}$), eccentricity ($\bar{e}$), inclination ($\bar{i}$), and RAAN deviation ($\Delta\overline{\Omega}$) are computed as

$$\bar{a} = \int_{t_s}^{t_f} a \, dt, \tag{84}$$

$$\bar{e} = \int_{t_s}^{t_f} e \, dt, \tag{85}$$

$$\bar{i} = \int_{t_s}^{t_f} i \, dt, \tag{86}$$

$$\Delta\overline{\Omega} = \int_{t_s}^{t_f} (\Omega - \Omega_d) \, dt, \tag{87}$$

where t_f is the final time, while t_s is conventionally set to 1 month, when the acquisition phase is completed. For each campaign, the mean values and standard deviations of each mean variable are provided. The run time associated with a single 1-year simulation is about 215 seconds on an Apple *M2 Pro* processor, 32 GB RAM, 10 cores (4 high-efficiency + 6 high-performance).

4.1. Target Orbit 1

Tables 2 and 3 collect the results for the first target orbit. Figures 2 and 3 show the time histories of the orbital elements, respectively, under no tolerances and when tolerances are included.
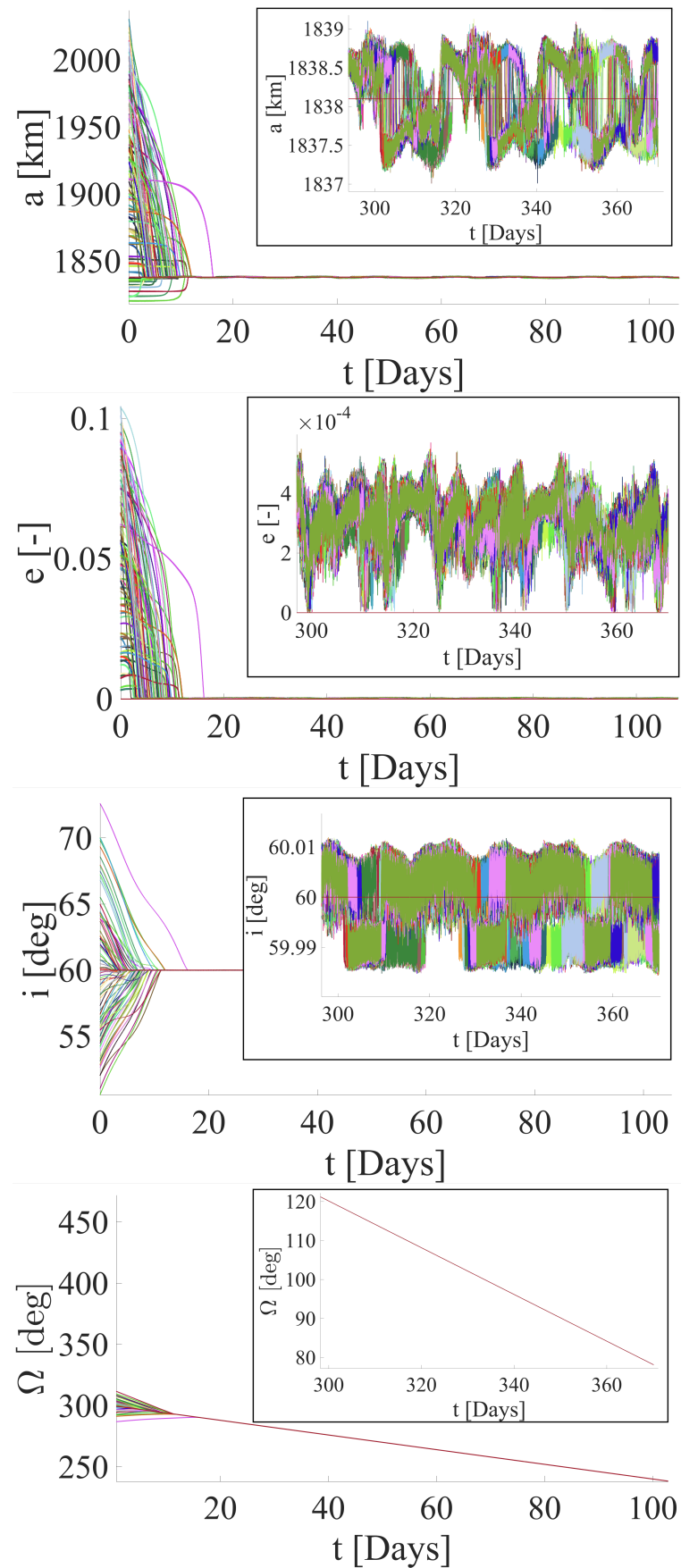
Figure 2. Target orbit 1, scenario 1 (no tolerance on orbit radius): orbit elements in the first 100 days (in the insets, zoom on the last days).
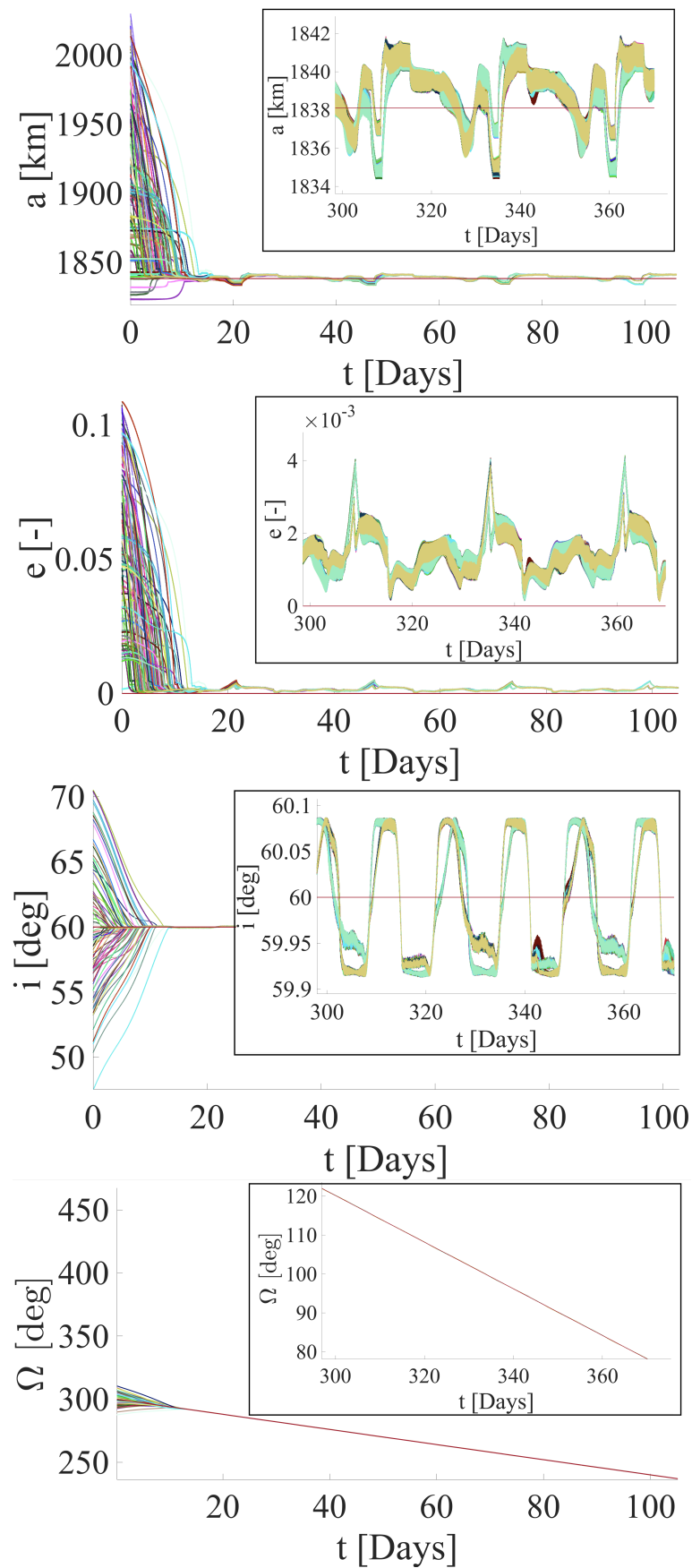
Figure 3. Target orbit 1, scenario 2 (tolerances on orbit radius): orbit elements in the first 100 days (in the insets, zoom on the last days).

Table 2. Results from Monte Carlo campaign—circular orbit.

Parameter	Mean Value	Standard Deviation
$\bar{a}$ [km]	1837.96	$4.83 \cdot 10^{-2}$
$\bar{e}$	$3.20 \cdot 10^{-4}$	$4.15 \cdot 10^{-6}$
$\bar{i}$ [deg]	59.99	$3.38 \cdot 10^{-5}$
$\Delta \bar{\Omega}$ [deg]	$4.87 \cdot 10^{-4}$	$9.15 \cdot 10^{-5}$
Final Mass Ratio	0.625	$5.29 \cdot 10^{-3}$

Table 3. Results from Monte Carlo campaign—elliptic orbit with assigned r_{Pmin} / r_{Amax}

Parameter	Mean Value	Standard Deviation
$\bar{a}$ [km]	1838.83	$3.38 \cdot 10^{-2}$
$\bar{e}$	$1.54 \cdot 10^{-3}$	$4.34 \cdot 10^{-6}$
$\bar{i}$ [deg]	59.99	$8.47 \cdot 10^{-6}$
$\Delta \bar{\Omega}$ [deg]	$8.63 \cdot 10^{-2}$	$8.63 \cdot 10^{-4}$
Final Mass Ratio	0.890	$2.94 \cdot 10^{-3}$

4.2. Target Orbit 2

Tables 4 and 5 collect the results for the second target orbit. Figures 4 and 5 show the time histories of the orbital elements, respectively, under no tolerances and when tolerances are included.

Table 4. Results from Monte Carlo campaign—circular orbit.

Parameter	Mean Value	Standard Deviation
$\bar{a}$ [km]	1838.33	$3.37 \cdot 10^{-3}$
$\bar{e}$	$3.11 \cdot 10^{-4}$	$1.80 \cdot 10^{-6}$
$\bar{i}$ [deg]	90.00	$2.45 \cdot 10^{-7}$
$\Delta \bar{\Omega}$ [deg]	$1.81 \cdot 10^{-4}$	$3.68 \cdot 10^{-7}$
Final Mass Ratio	0.661	$1.50 \cdot 10^{-3}$

Table 5. Results from Monte Carlo campaign—elliptic orbit with assigned r_{Pmin} / r_{Amax}

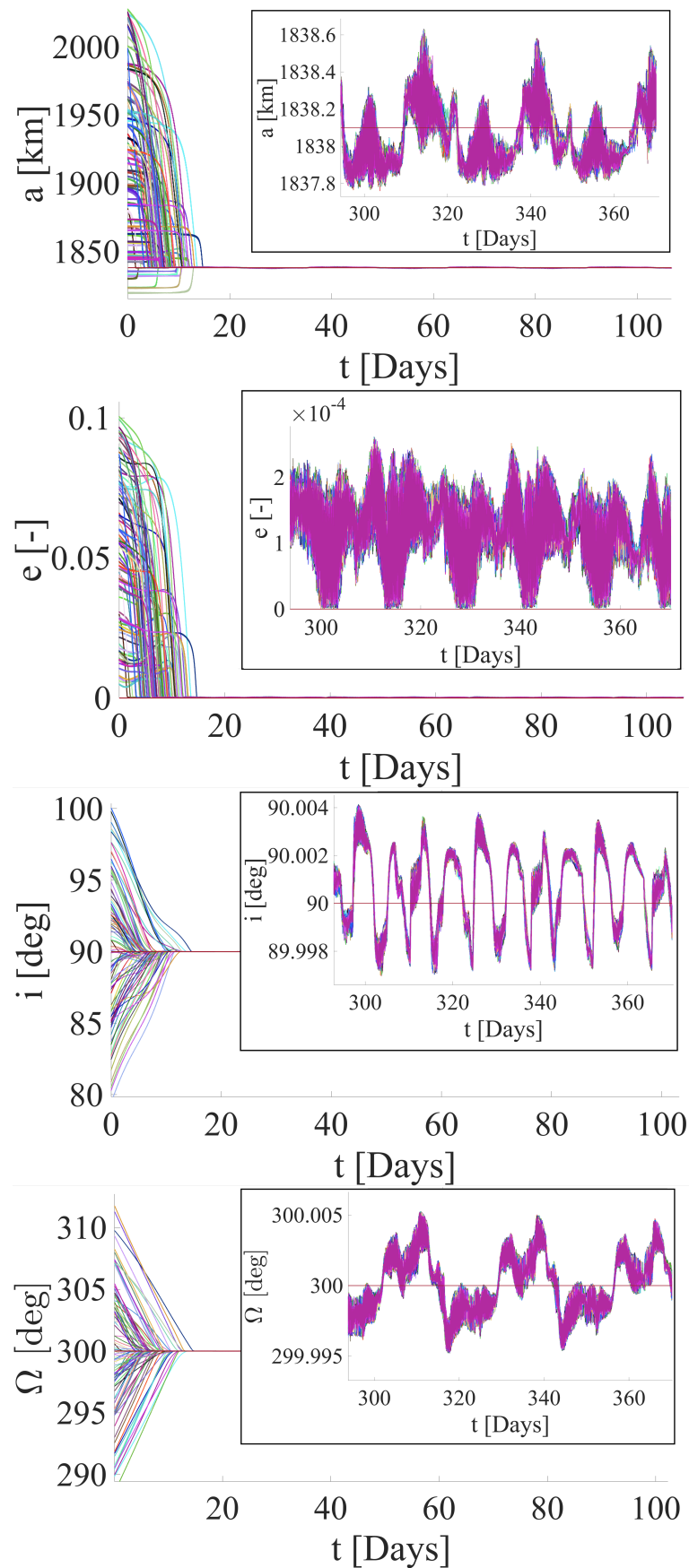| Parameter	Mean Value	Standard Deviation
$\bar{a}$ [km]	1837.34	$1.61 \cdot 10^{-1}$
$\bar{e}$	$2.31 \cdot 10^{-3}$	$6.41 \cdot 10^{-5}$
$\bar{i}$ [deg]	90.00	$7.43 \cdot 10^{-7}$
$\Delta \bar{\Omega}$ [deg]	$4.42 \cdot 10^{-4}$	$2.12 \cdot 10^{-6}$
Final Mass Ratio	0.911	$3.56 \cdot 10^{-3}$

Figure 4. Target orbit 2, scenario 1 (no tolerance on orbit radius): orbit elements in the first 100 days (in the insets, zoom on the last days).
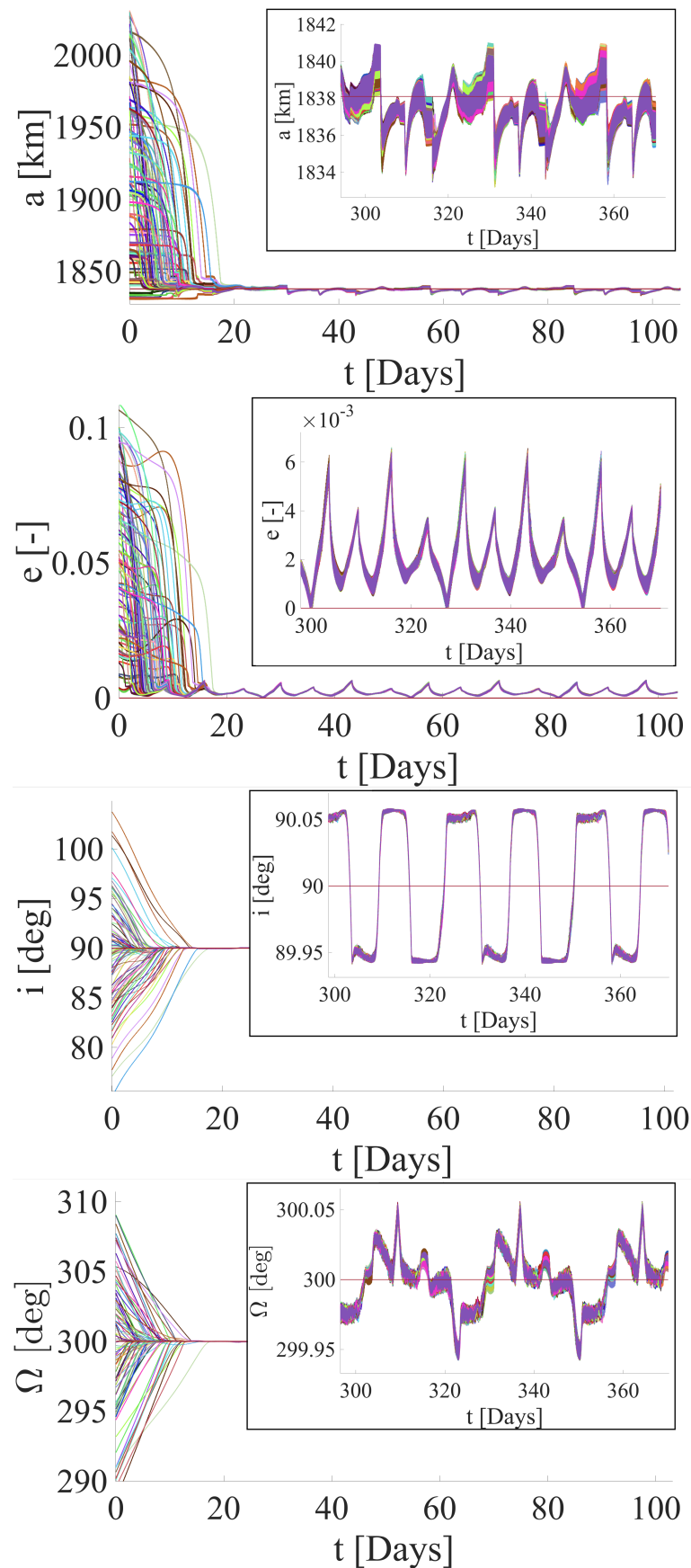
Figure 5. Target orbit 2, scenario 2 (tolerances on orbit radius): orbit elements in the first 100 days (in the insets, zoom on the last days).

5. Discussion of Results

From inspection of the results, it is evident that the proposed feedback control law is capable of adjusting the injection errors and keeping the spacecraft along the desired operational state, despite the active perturbations. In particular, in both operational scenarios the orbital elements are kept close to the desired value, with limited standard deviations. Unsurprisingly, when tolerances are introduced, the accuracy of the control law tends to decrease. For instance, the comparison between Figures 2a and 3a or between Figures 4a and 5a show that, when the constraint on the final orbit is relaxed, the oscillations in the semimajor axis are wider as expected, though very limited. However, despite a marginal increment in the error, the fuel saving is considerable, as the final mass ratio increases by 43% and 45%, respectively, for target orbit 1 and 2. The same considerations apply from inspection of Figures 2b–5b, by comparing the time histories of the eccentricity. Figures 2d and 4d highlight the capability of the control strategy at hand to keep the RAAN close to the desired value either when the secular variation vanishes or when the gravitational perturbations yield a near-linear drift.

Finally, Figure 6 depicts the time histories of the mass ratio for the first target orbit under the two operational scenarios. In both cases, the thrust is always on and at maximum value during the acquisition phase, and consequently, all the curves overlap, resulting in a global linear trend with respect to time. During the maintenance phase, the perturbation accelerations are comparable with the thrust acceleration. Therefore, when no tolerances are set, the thrust acceleration is variable. Instead, when tolerances are included, orbit maintenance is achieved through the succession of either zero thrust or variable thrust intervals, resulting in a shallow profile that mimics a step function. This results in a globally lower fuel expenditure.
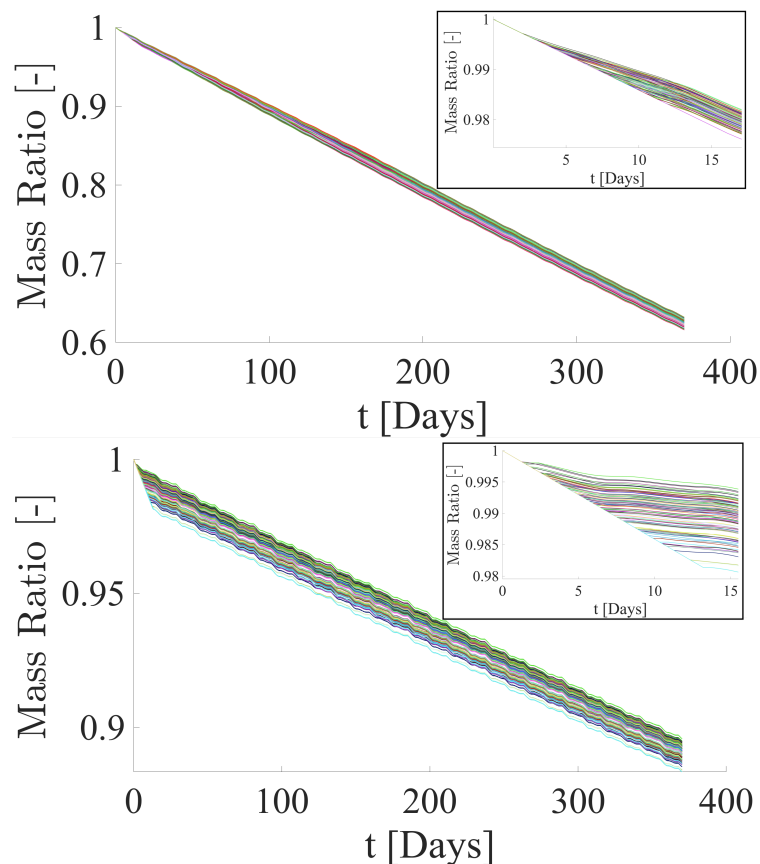

Figure 6. Time histories of the mass ratio for the first target orbit (in the insets, zoom on the acquisition phase). (**a**) Circular orbit. (**b**) Elliptic orbit with assigned r_{Pmin} / r_{Amax}.

6. Concluding Remarks

This research addresses the application of a Lyapunov feedback controller to inject a spacecraft into a very low lunar orbit, with subsequent maintenance maneuvers. The space vehicle is assumed to be equipped with a steerable and throttleable low-thrust engine. The formulation of the nonlinear constraints is simplified with respect to previous works by employing modified equinoctial elements. The stability analysis is developed in a general framework that includes time-varying orbit elements and proves that the asymptotic stability is quasi-global. Monte Carlo campaigns are carried out for two target orbits with different inclination and two operational scenario, i.e., a circular target orbit or an elliptic target orbit with assigned minimum radius at periselenium and maximum radius at aposelenium. The numerical simulations demonstrate the capability of the strategy at hand to perform orbit acquisition and maintenance despite third body and gravitational perturbations. Very-low-altitude lunar orbits with tight control of the orbit elements appear very attractive for the deployment of satellite constellations. Even though this research investigates operational scenarios with the only precession of the right ascension, the proposed feedback control law can be applied to target non-Keplerian trajectories with time-varying orbital elements.

Abbreviations

The following abbreviations are used in this manuscript:

RAAN	Right Ascension of the Ascending Node
MCI	Moon Centered Inertial
LVLH	Local Vertical Local Horizontal
LH	Local Horizontal

Appendix A. Planetary Data

Table A1 shows the gravitational parameters of the Sun, Earth, and Moon.

Table A1. Gravitational parameters.

Body	μ
Sun	132712440018
Earth	398600.4418
Moon	4902.7779

Table A2 shows the coefficients J_l of the zonal harmonics.

Table A2. Zonal harmonics of the selenopotential.

J_l	Value	J_l	Value
J_2	0.000203256369305959	J_{26}	$-2.2434487970911 \times 10^{-6}$
J_3	$8.59050334996568 \times 10^{-6}$	J_{27}	$4.61610568281654 \times 10^{-6}$
J_4	$-9.8522886746674 \times 10^{-6}$	J_{28}	$-6.7273906042203 \times 10^{-6}$
J_6	$-1.3293051175382 \times 10^{-5}$	J_{29}	$5.54940421259954 \times 10^{-6}$
J_7	$-2.2061158962342 \times 10^{-5}$	J_{31}	$-4.6246357265911 \times 10^{-6}$
J_8	$-9.4065451772204 \times 10^{-6}$	J_{33}	$-1.4141219096004 \times 10^{-6}$
J_9	$1.51243401890736 \times 10^{-5}$	J_{37}	$-1.6209625508441 \times 10^{-6}$
J_{10}	$3.89230799976237 \times 10^{-6}$	J_{39}	$1.29851648071154 \times 10^{-6}$
J_{11}	$5.14949783632897 \times 10^{-6}$	J_{42}	$-1.7804783918105 \times 10^{-6}$
J_{12}	$9.1117958405472 \times 10^{-6}$	J_{45}	$-1.4541586632206 \times 10^{-6}$
J_{16}	$-1.4596672751979 \times 10^{-6}$	J_{46}	$2.1351214383094 \times 10^{-6}$
J_{17}	$5.70913026297742 \times 10^{-6}$	J_{47}	$-1.9588420020059 \times 10^{-6}$
J_{20}	$-4.7874115985482 \times 10^{-6}$	J_{52}	$-1.3163362865652 \times 10^{-6}$
J_{22}	$2.97052872898108 \times 10^{-6}$	J_{54}	$1.26894455814441 \times 10^{-6}$
J_{23}	$1.75163995006724 \times 10^{-6}$	J_{66}	$-1.0675927011228 \times 10^{-6}$
J_{24}	$2.34692497584258 \times 10^{-6}$	J_{67}	$1.92342072984345 \times 10^{-6}$
J_{25}	$1.21874850482553 \times 10^{-6}$	J_{69}	$1.0580049555114 \times 10^{-6}$

Table A3 shows the coefficients J_{lm} and λ_{lm} of the sectoral and tesseral harmonics.

Table A3. Sectoral and tesseral harmonics of the selenopotential.

$J_{l,m}$	Value	$\lambda_{l,m}$	Value
$J_{2,2}$	0.000203256369305959	$\lambda_{2,2}$	0.000415878398442979
$J_{3,1}$	$8.59050334996568 \times 10^{-6}$	$\lambda_{3,1}$	0.20642811107848
$J_{3,2}$	$-9.8522886746674 \times 10^{-6}$	$\lambda_{3,2}$	0.16771320834929
$J_{3,3}$	$-1.3293051175382 \times 10^{-5}$	$\lambda_{3,3}$	-0.0496398759987853
$J_{4,1}$	$-2.2061158962342 \times 10^{-5}$	$\lambda_{4,1}$	2.86012534158749
$J_{4,2}$	$-9.4065451772204 \times 10^{-6}$	$\lambda_{4,2}$	-1.18630809022817
$J_{5,1}$	$1.51243401890736 \times 10^{-5}$	$\lambda_{5,1}$	-1.83532311833521
$J_{6,1}$	$3.89230799976237 \times 10^{-6}$	$\lambda_{6,1}$	-1.01434986302375
$J_{7,1}$	$5.14949783632897 \times 10^{-6}$	$\lambda_{7,1}$	-0.0229903684710072
$J_{9,1}$	$9.1117958405472 \times 10^{-6}$	$\lambda_{9,1}$	0.11842818400149
$J_{12,1}$	$-1.4596672751979 \times 10^{-6}$	$\lambda_{12,1}$	1.89596195628963

Appendix B. Sensitivity Analysis with Respect to the Gravitational Model

A sensitivity analysis is performed in order to assess the truncation error associated with the use of several harmonics of the selenopotential, as well as third- and fourth-body perturbations. Nominal simulations along the circular target orbit 1 are considered, while retaining an increasing number of harmonics in four different simulation setups: (i) harmonics associated with coefficients $|J_{lm}| > 10^{-5}$, i.e., four zonal harmonics and four sectoral/tesseral harmonics (compare Table A4); (ii) harmonics associated with coefficients $|J_{lm}| > 10^{-6}$, i.e., 34 zonal harmonics and 11 sectoral/tesseral harmonics (compare Table A5); (iii) harmonics up to order 50 (compare Table A6); (iv) harmonics up to order 100 (compare Table A7); (v) harmonics associated with coefficients $|J_{lm}| > 10^{-5}$ without third- and fourth-body effects (compare Table A8). From the inspection of Tables A4 through A8, it is apparent that for very-low-altitude lunar orbits, very accurate results can be obtained by including harmonics associated with coefficients $|J_{lm}| > 10^{-6}$.

Table A4. Case (i): final mass ratio is 0.617.

Parameter	Mean Value	Standard Deviation
a [km]	1838.04	5.18×10^{-1}
e	3.09×10^{-4}	6.70×10^{-5}
i [deg]	60.00	5.96×10^{-3}
$\Delta\Omega$ [deg]	1.56×10^{-2}	2.71×10^{-3}

Table A5. Case (ii): final mass ratio is 0.619.

Parameter	Mean Value	Standard Deviation
a [km]	1838.02	4.08×10^{-1}
e	3.25×10^{-4}	6.71×10^{-5}
i [deg]	60.00	5.75×10^{-3}
$\Delta\Omega$ [deg]	3.62×10^{-3}	2.84×10^{-3}

Table A6. Case (iii): final mass ratio is 0.618.

Parameter	Mean Value	Standard Deviation
a [km]	1838.01	3.82×10^{-1}
e	3.47×10^{-4}	9.23×10^{-5}
i [deg]	60.00	6.52×10^{-3}
$\Delta\Omega$ [deg]	1.01×10^{-3}	3.32×10^{-3}

Table A7. Case (iv): final mass ratio is 0.618.

Parameter	Mean Value	Standard Deviation
a [km]	1838.01	3.82×10^{-1}
e	3.47×10^{-4}	9.13×10^{-5}
i [deg]	60.00	6.75×10^{-3}
$\Delta\Omega$ [deg]	7.21×10^{-3}	3.40×10^{-3}

Table A8. Case (v): final mass ratio is 0.619.

Parameter	Mean Value	Standard Deviation
a [km]	1838.04	4.95×10^{-1}
e	3.06×10^{-4}	6.54×10^{-5}
i [deg]	60.00	5.65×10^{-3}
$\Delta\Omega$ [deg]	1.62×10^{-2}	2.85×10^{-3}

References

1. Fuller, S.; Lehnhardt, E.; Zaid, C.; Halloran, K. Gateway Program Status and Overview. In Proceedings of the 72nd International Astronautical Congress, Dubai, United Arab Emirates, 25–29 October 2021.
2. Lara, M. Design of long-lifetime lunar orbits: a hybrid approach. *Acta Astronaut.* **2011**, *69*, 186–199.
3. Nie, T.; Gurfil, P. Lunar frozen orbits revisited. *Celest. Mech. Dyn. Astron.* **2018**, *130*, 61.
4. Pontani, M.; Di Roberto, R.; Graziani, F. Lunar orbit dynamics and maneuvers for Lunisat missions. *Acta Astronaut.* **2018**, *149*, 111–122.
5. Singh, S.K.; Woollands, R.; Taheri, E.; Junkins, J. Feasibility of quasi-frozen, near-polar and extremely low-altitude lunar orbits. *Acta Astronaut.* **2020**, *166*, 450–468.
6. Liu, J.; Xu, B.; Li, C.; Li, M. Lifetime Extension of Ultra Low-Altitude Lunar Spacecraft with Low-Thrust Propulsion System. *Aerospace* **2022**, *9*, 305.
7. LaFarge, N.B.; Miller, D.; Howell, K.C.; Linares, R. Guidance for closed-loop transfers using reinforcement learning with application to libration point orbits. In Proceedings of the AIAA Scitech 2020 Forum, Orlando, FL, USA, 6–10 January 2020; p. 458.

8. Hart, J.; King, E.; Miotto, P.; Lim, S. Orion GN&C architecture for increased spacecraft automation and autonomy capabilities. In Proceedings of the AIAA Guidance, Navigation and Control Conference and Exhibit, Honolulu, HI, USA, 16–21 August 2008; p. 7291.

9. LaFarge, N.B.; Miller, D.; Howell, K.C.; Linares, R. Autonomous closed-loop guidance using reinforcement learning in a low-thrust, multi-body dynamical environment. *Acta Astronaut.* **2021**, *186*, 1–23.

10. Conway, B.A. A survey of methods available for the numerical optimization of continuous dynamic systems. *J. Optim. Theory Appl.* **2012**, *152*, 271–306.

11. Leomanni, M.; Bianchini, G.; Garulli, A.; Giannitrapani, A. A class of globally stabilizing feedback controllers for the orbital rendezvous problem. *Int. J. Robust Nonlinear Control.* **2017**, *27*, 4607–4621.

12. Kluever, C.A. Simple guidance scheme for low-thrust orbit transfers. *J. Guid. Control. Dyn.* **1998**, *21*, 1015–1017.

13. Gurfil, P. Nonlinear feedback control of low-thrust orbital transfer in a central gravitational field. *Acta Astronaut.* **2007**, *60*, 631–648.

14. Chang, D.E.; Chichka, D.F.; Marsden, J.E. Lyapunov-based transfer between elliptic Keplerian orbits. *Discret. Contin. Dyn. Syst. Ser. B* **2002**, *2*, 57–68.

15. Leeghim, H.; Cho, D.H.; Jo, S.J.; Kim, D. Generalized guidance scheme for low-thrust orbit transfer. *Math. Probl. Eng.* **2014**, *2014*, 407087.

16. Federici, L.; Benedikter, B.; Zavoli, A. Deep learning techniques for autonomous spacecraft guidance during proximity operations. *J. Spacecr. Rocket.* **2021**, *58*, 1774–1785.

17. Izzo, D.; Öztürk, E. Real-time guidance for low-thrust transfers using deep neural networks. *J. Guid. Control. Dyn.* **2021**, *44*, 315–327.

18. Capra, L.; Brandonisio, A.; Lavagna, M. Network architecture and action space analysis for deep reinforcement learning towards spacecraft autonomous guidance. *Adv. Space Res.* **2023**, *71*, 3787–3802.

19. Petropoulos, A.E. Refinements to the Q-Law for the Low-Thrust Orbit Transfers In Proceedings of the 15th AAS/AIAA Space Flight Mechanics Conference, Copper Mountain, CO, USA, 23–27 January 2005.

20. Narayanaswamy, S.; Damaren, C.J. Equinoctial Lyapunov control law for low-thrust rendezvous. *J. Guid. Control. Dyn.* **2023**, *46*, 781–795.

21. Peterson, J.T.; Arya, V.; Junkins, J.L. Connecting the Equinoctial Elements and Rodrigues Parameters: A New Set of Elements. *J. Guid. Control. Dyn.* **2023**, *46*, 1726–1744.

22. Pontani, M.; Pustorino, M. Nonlinear Earth orbit control using low-thrust propulsion. *Acta Astronaut.* **2021**, *179*, 296–310.

23. Pontani, M.; Teofilatto, P. Deployment strategies of a satellite constellation for polar ice monitoring. *Acta Astronaut.* **2022**, *193*, 346–356.

24. Pontani, M.; Pustorino, M. Low-Thrust Lunar Capture Leveraging Nonlinear Orbit Control. *J. Astronaut. Sci.* **2023**, *70*, 28.

25. Battin, R.H. *An Introduction to the Mathematics and Methods of Astrodynamics*; AIAA: Reston, VA, USA, 1999.

26. Giorgi, S. *Una Formulazione Caratteristica del Metodo Encke in Vista Dell'Applicazione Numerica*; Università di Roma, Scuola di Ingegneria Aerospaziale: Rome, Italy, 1964.

27. Konopliv, A.; Asmar, S.; Carranza, E.; Sjogren, W.; Yuan, D. Recent gravity models as a result of the Lunar Prospector mission. *Icarus* **2001**, *150*, 1–18.

28. Curtis, H. *Orbital Mechanics for Engineering Students*; Butterworth-Heinemann: Oxford, UK, 2013.

29. Wolfram Mathematica. 2023. Available online: https://www.wolfram.com/mathematica/ (accessed on).